Earth Planet. Sci. Lett. 669 (2025) 119573

Contents lists available at ScienceDirect

Earth and Planetary Science Letters

journal homepage: www.elsevier.com/locate/epsl

Frictional stability of Pelona–Orocopia–Rand schists under hydrothermal conditions and implications for seismic hazards in Southern California

S.E. Guvercin [a,*], S. Barbot [a], L. Zhang [b,*], Z. Yang [b], J. Platt [a], C. Seyler [a], N. Phillips [a]

[a] Department of Earth Sciences, University of Southern California, 3651 Trousdale Pkwy, Los Angeles, CA 90089, USA
[b] Institute of Geology, China Earthquake Administration, Chaoyang, Beitucheng W Rd, Beijing, 100017, China

ARTICLE INFO

Editor: J.P. Avouac

ABSTRACT

The Pelona–Orocopia–Rand (POR) schists were emplaced during the Farallon flat subduction in the early Cenozoic and now occupy the root of major strike-slip faults of the San Andreas Fault system. The POR schists are considered frictionally stable at lower temperatures than other basement rocks, limiting the maximum depth of seismicity in Southern California. However, experimental constraints on the composition and frictional properties of POR schists are still missing. Here, we study the frictional behavior of synthetic gouge derived from Pelona, Portal, and Rand Mountain schist wall rocks under hydrothermal, triaxial conditions. We conduct velocity-step experiments from 0.04 to 1 μm/s from room temperature to 500 °C under 200 MPa effective normal stress, including a 30 MPa pore-fluid pressure. The frictional stability of POR schists in the lower crust is caused by a thermally activated transition from slip-rate- and state-dependent friction to inherently stable, rate-dependent creep between 300 °C and 500 °C, depending on sample composition and slip-rate. The mineralogy of POR schists shows much variability caused by different protoliths and metamorphic grades, featuring various amounts of phyllosilicates, quartz, feldspar, and amphibole. Pelona and Portal schists exhibit a velocity-weakening regime enabling the nucleation and propagation of earthquakes when exhumed in the middle crust, as in the Mojave section of the San Andreas Fault. The contrasted frictional properties of POR schists exemplify the lithological control of seismic processes and associated hazards.

Plain language summary

Despite their critical importance in controlling seismicity, the frictional properties of rocks in Southern California are poorly known. Here, we investigate the mechanical properties of the Pelona–Orocopia–Rand (POR) schists that surround major Southern California faults at middle and lower-crustal depths. We deform powders derived from country rocks in Sierra Pelona, Portal Ridge, and Rand Mountain under controlled pore-fluid pressure and temperature conditions. We explain the laboratory observations with empirical and physical models of rock friction. All samples feature stable, velocity-strengthening behavior above 500 °C at slip-rates relevant to earthquake nucleation due to the activation of flow-like deformation at high temperatures. However, the synthetic gouges derived from the Sierra Pelona and Portal schists feature a frictionally unstable regime enabling the nucleation of large earthquakes in the middle crust. The stability of POR schists in the lower crust is caused by a thermally activated brittle-to-flow transition at 300-500 °C, depending on sample composition and slip-rates. The varied frictional behaviors of POR schists help us better understand how different rock types influence earthquake size and recurrence patterns in the continental crust.

1. Introduction

The seismogenic behavior of faults is modulated by the mechanical properties of the host rocks under their ambient barometric and hydrothermal conditions (e.g., Niemeijer et al., 2016; Okuda et al., 2023; Barbot and Zhang, 2023; den Hartog et al., 2012; Blanpied et al., 1995; Carpenter et al., 2012). Unraveling the frictional properties of rocks in their natural environment is key to devising increasingly accurate models of seismicity (Barbot et al., 2012; Barbot, 2020; Julve et al., 2023; Wang and Barbot, 2024; Julve et al., 2025). In the continental crust, this task is made particularly challenging due to the lithological complexity inherited from a prolonged geological history, involving several overprinting stages of magmatism, sedimentation, and metamorphism (e.g., Romanyuk et al., 2007). Various processes, including accretion, obduc-

* Corresponding authors.
E-mail addresses: guvercin@usc.edu (S.E. Guvercin), zhanglei@ies.ac.cn (L. Zhang).

https://doi.org/10.1016/j.epsl.2025.119573
Received 29 November 2024; Received in revised form 3 July 2025; Accepted 2 August 2025

Available online 11 August 2025

tion, or underplating result in mineralogical compositions ranging from felsic to mafic throughout the continental crust (e.g., Hawkesworth and Kemp, 2006). This compositional diversity plays an important role in shaping the mechanical and thermal properties of the crust, affecting the overall seismic potential (Rudnick and Gao, 2014; Christensen and Mooney, 1995).

The bulk seismogenic properties of the continental crust can be inferred from laboratory experiments on quartz-rich rocks, which exhibit unstable friction from 50 °C to 450 °C under high pore-fluid pressure (Blanpied et al., 1995, 1998; Lei et al., 2024), overall compatible with the depth of seismicity in California (Nazareth and Hauksson, 2004, e.g.,). However, variable protoliths (Tulley et al., 2022), degree of metamorphism and metasomatism (Ujiie et al., 2022), and fluid-rock interactions (e.g., Carpenter et al., 2022) may produce significant variability in mechanical properties of fault zones (Moore and Lockner, 2011; Zhang and He, 2013; Zhang et al., 2019; Okuda et al., 2021). A detailed understanding of fault behavior requires investigation of local rocks.

The California margin forms an ideal natural laboratory for exploring how compositional heterogeneity affects the thermo-mechanical properties of continental transforms. California exhibits several different geomorphic provinces from its subduction origin, featuring a forearc accretionary wedge in the Coast Ranges and offshore Patton escarpment, a forearc basin in the Great Central Valley, and arc magmatism in Sierra Nevada. This tectonic setting is now traversed by well-developed strike-slip fault systems, including the San Andreas Fault (SAF), the Eastern California Shear Zone, and the Walker Lane, which are responsible for elevated seismic hazards (e.g., Field et al., 2017).

Deformation experiments on talc and tremolite schists from the Franciscan Complex, Central California (Hirauchi et al., 2020), and on lawsonite blueschist from the Franciscan belt, Tiburon Peninsula (Sawai et al., 2016) reveal the complex temperature, slip-rate, and pressure dependence of the frictional resistance of deep subduction rocks. Laboratory experiments on borehole samples from the San Andreas Fault Observatory at Depth (SAFOD) provide insights into the strength and healing behavior of the SAF at shallow depths (e.g., Carpenter et al., 2009, 2015; Moore et al., 2016), explaining the presence of the central creeping section by the frictional properties of phyllosilicates at low temperature (Ikari et al., 2009; Nie and Barbot, 2024). Despite this important work, very little is known about the frictional behavior of the remaining country and fault rocks in California.

In large swaths of Southern California, the lower continental crust was formed by the accretion of the Pelona–Orocopia–Rand (POR) schists during the flat subduction of the Farallon plate that transported trench sediments in the greenschist and blueschist facies (Jacobson et al., 2007; Chapman, 2016; Chapman et al., 2010). The POR schists now underlie the San Gabriel Mountains, the Sierra Nevada, the western Mojave block, and the Rand Mountains at mid- to lower-crustal depths (Jacobson et al., 2007; Chapman, 2016; Chapman et al., 2010; Eymold and Jordan, 2019; White et al., 2021), forming the host rocks of the Mojave section of the San Andreas Fault and of major strike-slip faults in the Eastern California Shear Zone (Fig. 1). The POR schists are identified as a widespread unit at mid-crustal depths in the Mojave, Salinia, and San Gabriel provinces in the Community Rheology Model of the Statewide California Earthquake Center (Hearn et al., 2020) (Fig. 1c). The distribution of POR schists in mid-crust is inferred by seismic imaging, whereby spatial variations in seismic velocities and seismic reflectors betray differences in lithology and degree of metamorphism beneath the San Gabriel Mountains, Sierra Nevada, western Mojave block, and Rand Mountains (e.g., Fuis et al., 2005; Lee et al., 2014; White et al., 2021). Seismic anisotropy caused by the strong fabric alignment of sheet silicates further supports the emplacement of the POR schists at mid-crustal depths (e.g., Porter et al., 2011; Wang et al., 2020).

The presence of a POR schist basement is believed to reduce the maximum depth of seismicity in Southern California due to the onset of plasticity at lower temperature than for other basement rocks based on their assumed elevated concentrations of quartz and micas (Magistrale and Zhou, 1996). However, experimental constraints on the composition and frictional properties of POR schists are still missing. In this study, we document the varied composition and frictional properties of representative POR schist samples under hydrothermal and triaxial conditions to constrain fault behavior and seismic potential at mid- to lower-crustal depths. To illustrate the heterogeneity in mechanical properties, we focus on samples from Sierra Pelona, Portal Ridge, and Rand Mountain, here referred to as Pelona schist, Portal schist, and Rand schist, capturing different relevant protoliths and metamorphic grades. We first conduct X-Ray Diffraction (XRD) and thin section analyses to document the compositional heterogeneity of POR schists. We then perform velocity-step experiments from room temperature to 500 °C under 200 MPa effective normal stress and capture the mechanical properties of POR schists using empirical and physical models of fault friction. The Pelona and Portal schists exhibit steady-state velocity-weakening friction at temperatures that overlap with the unstable regime of Westerly granite in wet conditions (Blanpied et al., 1995). In contrast, the Rand schist sample features velocity-strengthening at all the experimental temperatures and slip-rates considered. The stable behavior of POR schists at mid- and lower-crustal depths is caused by a thermally activated transition to rate-dependent creep between 300 and 500 °C, depending on sample composition. Our study highlights the compositional origin of mechanical heterogeneity in the middle to lower crust.

2. Pelona–Orocopia–Rand schist samples

The POR schists originated in the Late Cretaceous to early Cenozoic from the shallow subduction of the Farallon plate (Jacobson et al., 2007; Grove and Bebout, 1995; Saleeby, 2003) and now crop out at various isolated places in Central and Southern California (Fig. 1b). Based on metamorphic and compositional characteristics, the northern cluster includes outcrops from the San Emigdio Mountains, Tehachapi Mountains, Rand Mountains, Sierra de Salinas, and Portal Ridge. The southern cluster encompasses outcrops from Mount Pinos and Sierra Pelona to the Orocopia Mountain and Cemetery Ridge (Chapman, 2016). The Rand Mountain and Sierra de Salinas schists were deposited and metamorphosed approximately 10–20 million years earlier than the Pelona and Orocopia schists and generally exhibit a higher metamorphic grade than the Pelona and Orocopia varieties from the southern cluster (Chapman, 2016).

We focus on the mechanical properties and composition of the POR schists in Southern California from Sierra Pelona (southern cluster), Portal Ridge, and Rand Mountains (northern cluster), representing both groups with distinct metamorphic grades. The Pelona schists exhumed from beneath the San Gabriel Mountains driven by extensional processes and reached peak metamorphism at ~520 °C and 1 GPa by ~60 Ma (Jacobson, 1990; Xia and Platt, 2017). The Portal schists were deposited around 80 Ma, metamorphosed at 700 °C, and uplifted by ~70 Ma, sharing arc-related origins and zircon ages with the Sierra de Salinas schists (Grove et al., 2003; Chapman, 2016). The Rand schists deposited after 85 Ma, with peak metamorphism at ~556 °C and 890-940 MPa (Chapman, 2016, e.g.,).

We consider several samples from Sierra Pelona, Portal Ridge, and Rand Mountains (Fig. 2). We first examine the compositional heterogeneities of Pelona and Rand schists using samples PLS2, PLS3, and PLS5 from Sierra Pelona and samples RM1, RM3, RM4, RM5, and RM7 from Rand Mountains. The XRD and thin section analysis of PLS2, POS, and RM5 provide insights into their distinct mineralogical compositions and origins (Table 1, Figs. S1, S2 & S3). We determine the frictional properties of the PLS2, POS, and RM5 samples, which feature contrasting mineralogical composition, protolith, and metamorphic grade, allowing us to document the possible range of mechanical behaviors of POR schists.

PLS2 is a mafic schist of volcanic origin, with a dominant composition of chlorite and amphiboles. The quartz in PLS2 is highly deformed. Minor amounts of hematite, twinned albite, and epidote are also present

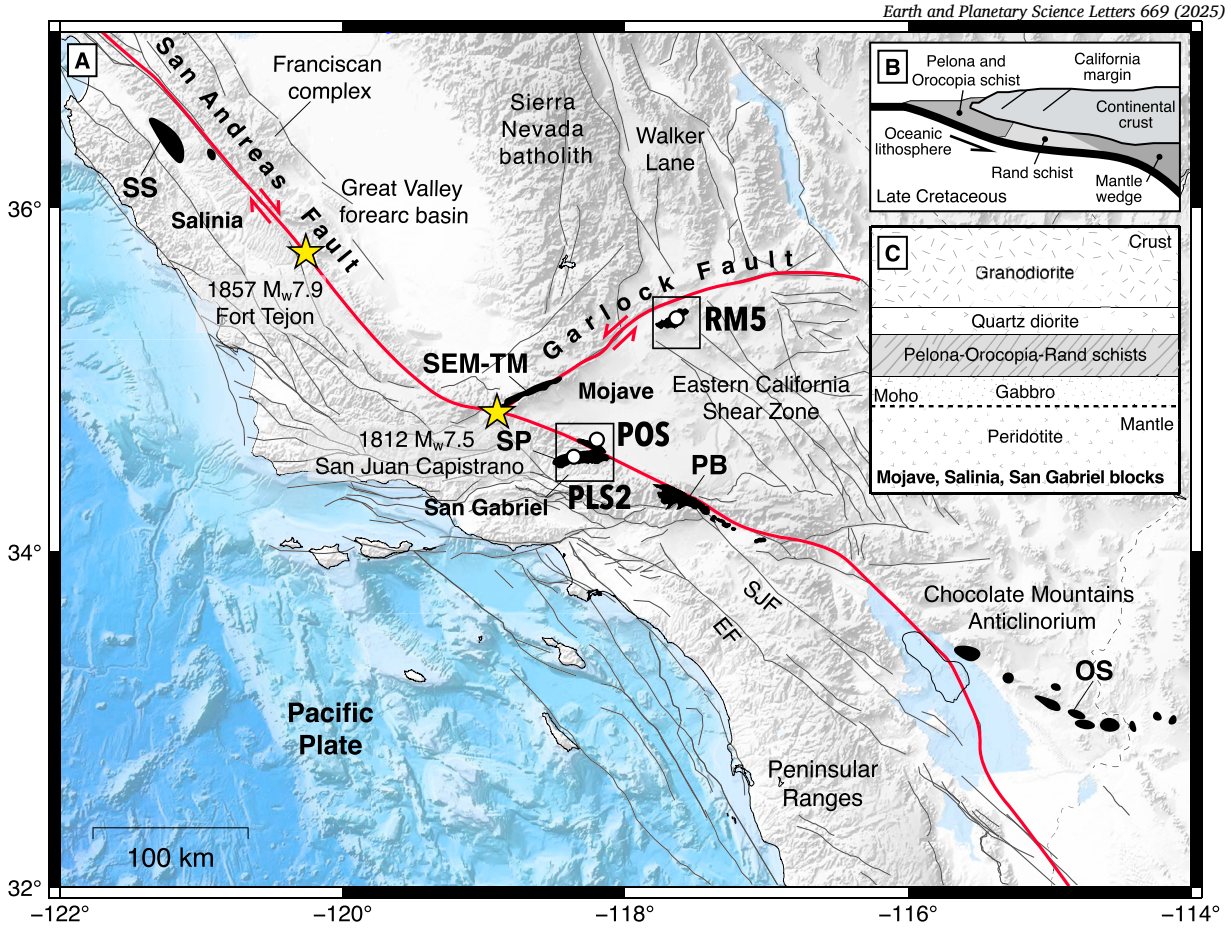

Fig. 1. Seismo-tectonic map of Southern California. a) Major tectonic features and fault systems. The sample locations of PLS2, POS, and RM5 schists are marked with circles. The Patton Escarpment is the relic trench of the Farallon subduction. Black shaded areas show the surface outcrops of POR schist. Possible epicenters of 1812 Mw 7.5 San Juan Capistrano and 1857 Mw 7.9 Fort Tejon earthquakes are marked by stars. White and blue shades indicate corresponding surface ruptures. Black squares indicate the regions shown in Fig. 2. b) Possible scenario of POR schist emplacement starting in the late Cretaceous (Chapman, 2016). c) Simplified depth-dependent lithological model of the Mojave, San Gabriel, and Salinia blocks (Hearn et al., 2020). Faults: EF, Elsinore Fault; SJF, San Jacinto Fault. Schist outcrops: SS, Sierra de Salinas; SP, Sierra Pelona; EF, East Fork; BR, Blue Ridge; OS, Orocopia Schist; SEM, San Emigdio Mountains; TM, Tehachapi Mountains.

(Fig. 3a-b). In contrast, POS is rich in quartz and albite, with substantial amounts of biotite and almandine. The presence of iron-rich garnet (almandine) and graphite, originally from organic matter, further suggests a clay-rich sedimentary protolith for POS, for example, a shale (Fig. 3c-d). RM5 is a calcium-rich mafic schist, presumably metabasalt, with a significant presence of chlorite and amphiboles along with large epidote crystals, calcite, a small amount of quartz and a higher amount of albite compared to PLS2 and POS. Chlorite is widely distributed throughout RM5 (Fig. 3e-f).

PLS3 is a metasedimentary schist dominated by 27 wt% albite, 57 wt% quartz, and 16 wt% muscovite, with minor amounts of epidote, biotite, and garnet, reflecting its high-pressure metamorphic origins. The presence of blue amphiboles suggests that PLS3 experienced significant pressure, similar to subduction-related metamorphism. In contrast, PLS5 is a mafic schist with a high chlorite content (53 wt%) and substantial actinolite (29 wt%), indicating a lower pressure but more mafic composition with inclusions of epidote, albite, and minor biotite. Although PLS5 shares the mafic composition and chlorite dominance with PLS2, PLS3 differs significantly, being more felsic with higher albite and quartz content.

RM1 is a metasomatic, altered metasediment with 45 wt% albite, 26 wt% quartz, and 17 wt% chlorite, showing twinning in albite and minor garnet and biotite, partly altered to chlorite. RM3, on the other hand, is amphibole-rich, with 88 wt% actinolite. RM4 presents a more complex texture with a mix of large albite crystals and inclusions of actinolite and epidote, indicating a high degree of deformation and complicated metamorphic history. RM7, a metasedimentary schist, contains significant albite, biotite, and quartz, with biotite altered to chlorite. RM1 through RM7 show varying compositions but generally exhibit more felsic and metasedimentary characteristics, while RM5 stands out with its more mafic and calcic composition and greater chlorite content. Fig. 4 shows the thin sections of samples PLS3, PLS5, RM1, RM3, RM4 and RM7 with labeled minerals.

Despite their proximity, the composition of POR schists varies significantly, reflecting the diverse protoliths and the range of metamorphic conditions experienced during burial and exhumation. This variability documents the heterogeneity inherent in the continental crust, where a diverse lithological history contributes to variations in mechanical and thermal properties. Additional mineral alteration may occur in active fault zones. Such compositional diversity may play an important role in shaping the seismic behavior of the continental crust.

3. Triaxial deformation experiments

We determine the frictional properties of POR schists using samples POS from Portal Ridge, PLS2 from Sierra Pelona, and RM5 from the Rand Mountains, postponing mechanical tests on the remaining samples to future work. We conduct experiments using a triaxial testing apparatus under a nominal effective normal stress of 200 MPa and a pore fluid pressure of 30 MPa, simulating pressure–temperature conditions representative of mid- to lower-crustal depths. We conduct all experiments from room temperature to 500 °C by steps of 100 °C. The experiments

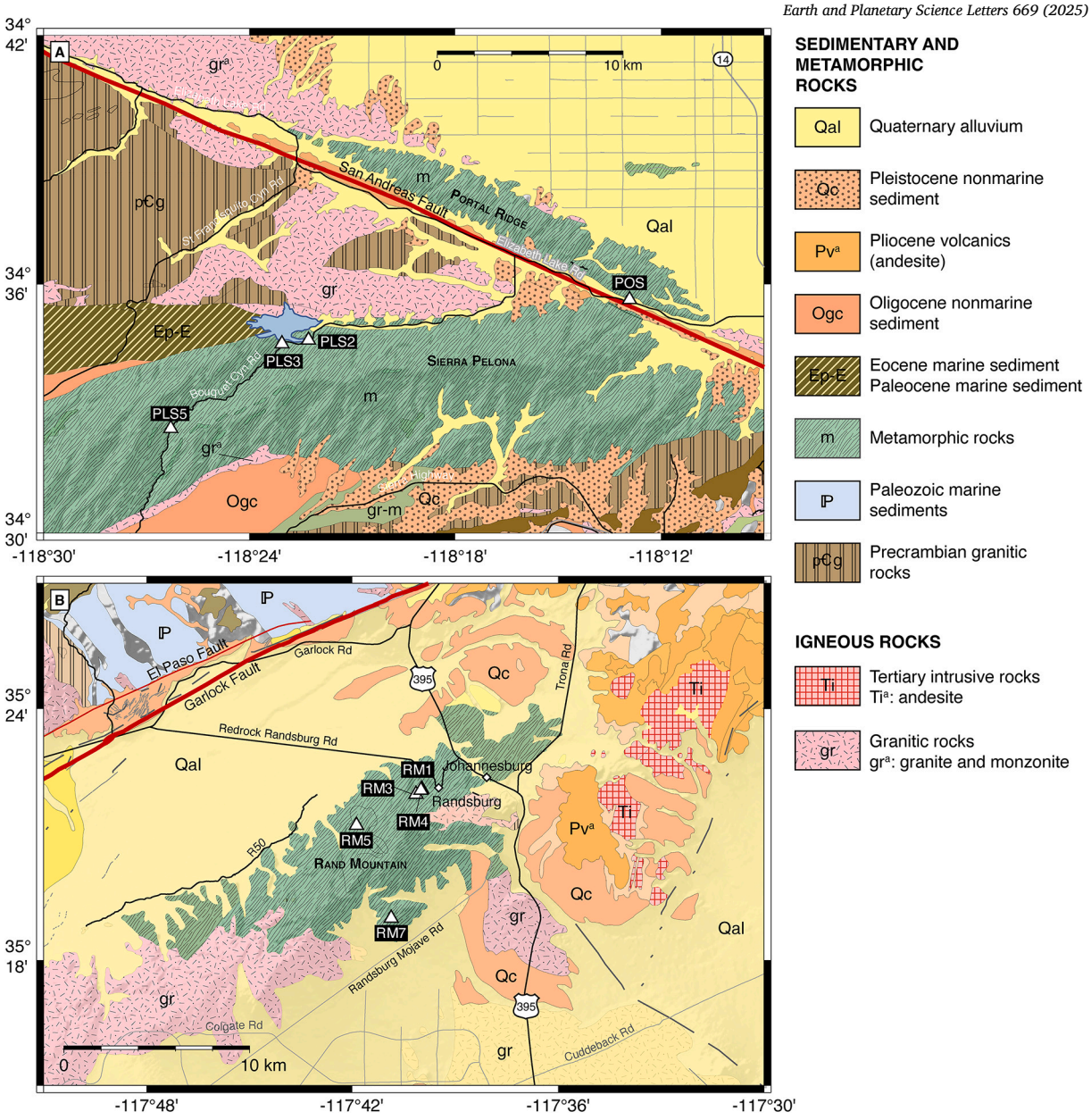

Fig. 2. Geological setting of the Pelona, Portal, and Rand schists in Southern California. a) Location of the Pelona schist samples along Bouquet Canyon Rd and the Portal schist sample along Elizabeth Lake Rd. b) Location of the Rand schist samples along R83. See coordinates in Table 1. All samples are collected in the metamorphic unit (green). The samples exhibit much compositional variability despite their proximity. Modified from Jenkins (1977).

Table 1
Location and mineral composition of POR schist samples from Portal Ridge (POS), Sierra Pelona (PLS2, PLS3, and PLS5), and Rand Mountains (RM1, RM3, RM4, RM5, and RM7) (with an uncertainty of 5 wt%). The samples subject to triaxial deformation are indicated by *. Felspars encompass K-feldspar (microline), Na-feldspar (albite), and Ca-feldspar (anorthite). Act: Actinolite (fibrous amphibole), Amph: Amphibole, Chl: Chlorite, Cln: Clinochlore (magnesium-rich chlorite), Ep: Epidote, Hbl: Hornblende, Mcc: Microcline, Qtz: Quartz, Ab: Albite, Bt: Biotite, Ms: Muscovite, Cumm: Cummingtonite, Ttn: Titanite, Alm: Almandine (iron-rich garnet).

Sample	Longitude	Latitude	Cln	Chl	Ab	Qtz	Ms	Act	Mcc	Bt	Amp	Ep	Cumm	Ttn	Alm
POS*	-118.21529	34.59391		5%	10%	60%				20%					5%
PLS2*	-118.37128	34.57762		40%	5%	5%		45%				5%			
PLS3	-118.38419	34.57613			27%	57%	16%								
PLS5	-118.43824	34.54207	53%		6%			29%	11%	2%					
RM1	-117.66622	35.36806	17%		45%	26%	4%		6%		2%				
RM3	-117.66912	35.36606	12%					88%							
RM4	-117.66667	35.36767	5%		21%			74%							
RM5*	-117.69800	35.35370		20%	15%	< 5%					40%	10%	10%	< 5%	
RM7	-117.68114	35.31668	4%		33%	32%		3%		28%					

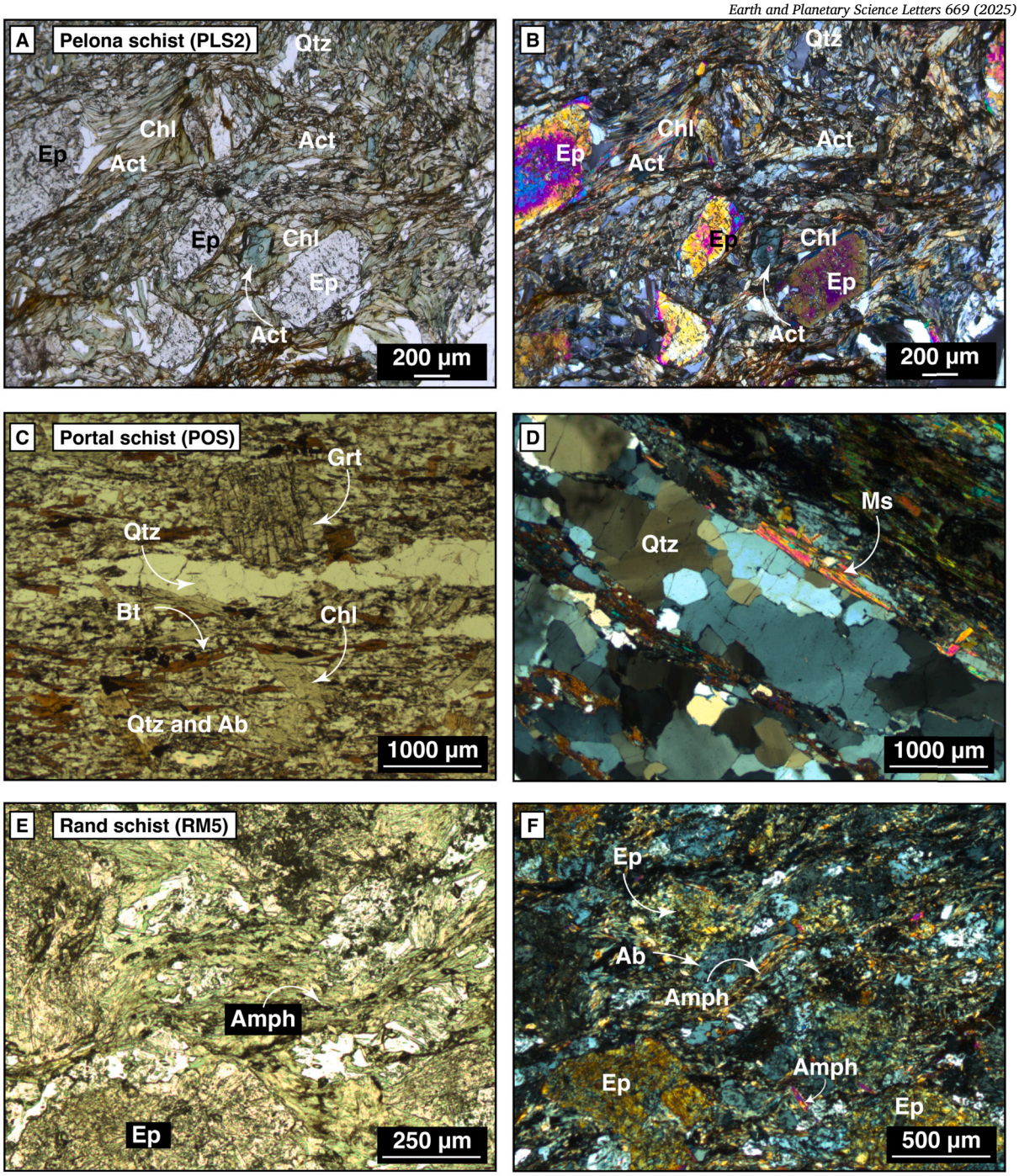

Fig. 3. Thin section analysis of Pelona (PLS2), Portal (POS), and Rand (RM5) schist samples under plane-polarized (left) and cross-polarized (right) light. Act: Actinolite, Amph: Amphibolite, Chl: Chlorite, Ep: Epidote, Qtz: Quartz, Ab: Albite, Bt: Biotite, Ms: Muscovite.

are performed on cylindrical gabbro samples with a saw cut fault inclined at 35°. The edges of both gabbro blocks are roughened by 200# abrasive and the surfaces are roughened by emery powder. To improve the access of pore fluid to the gouge, we use two holes in the upper block. Each hole in the upper block is filled with a brass filter to avoid intrusion of gouge. All the samples are crushed and sieved into < 200 µm grain size powder and mixed with deionized water to form a paste. The paste is then spread 1 mm thick on the cylindrical gabbro block and tucked against the bottom block. The gouge is then placed into a 24 mm copper jacket. The jacket is filled with alumina and carbide blocks symmetrically around the saw-cut gabbro blocks. We use double O-ring seals at the bottom and top of the jacket to isolate the content of the jacket. Finally, the jacket is connected to the furnace, filled with boron-nitride, and sealed with boron-nitride-saturated cotton to prevent heat leaks. A diagram of the experimental setup is shown in Fig. S5. More details of the experimental setup can be found in He et al. (2006).

We maintain the pore-fluid pressure, confining pressure, and temperature constant and observe the evolution of shear stress versus displacement during velocity steps. Due to the coupling between shear and normal stress in a triaxial setting, the effective normal stress increases from 200 to about 220 MPa with increasing slip. We measure the velocity dependence of the friction coefficient, defined as the ratio of shear stress to effective normal stress, accounting for the effect of pore-fluid pressure, during stepwise variations of loading rate in two sequences with axial loading rates of 0.04 µm/s, 0.2 µm/s, and 1.0 µm/s. For each velocity, the axial displacement is 0.2 mm. During post-processing, we

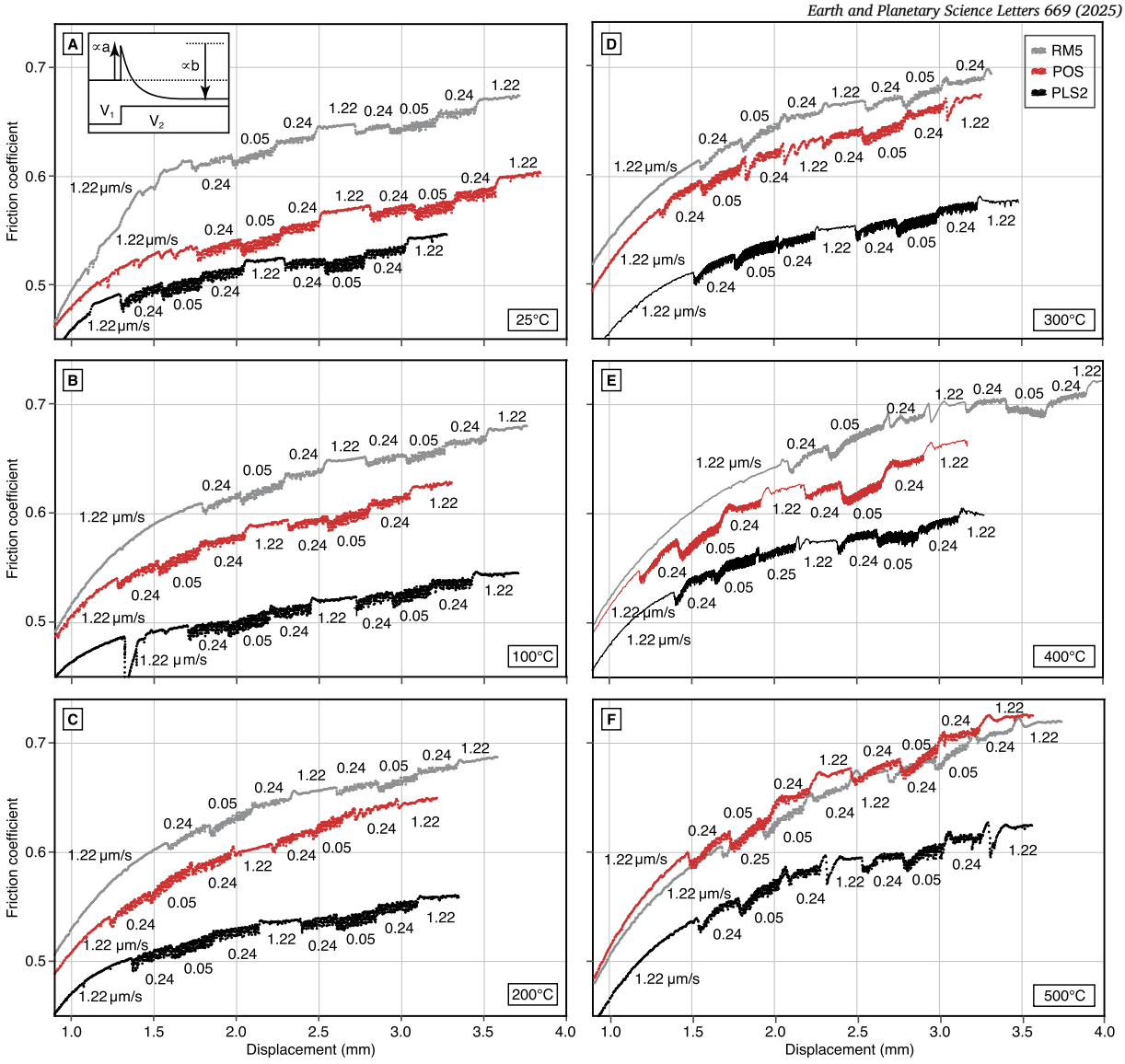

Fig. 4. Evolution of the friction coefficient of POR schists during velocity steps at various temperatures and slip-rates. Sequence of velocity steps at a) 25°C, b) 100°C, c) 200°C, d) 300°C, e) 400°C, and f) 500°C. Pelona schist (PLS2), Portal schist (POS), and Rand schist (RM5) gouge are shown in black, red, and gray. The inset represents the expected mechanical response at high machine stiffness during a velocity step. With low machine stiffness, the system response is more gradual and may involve oscillations and stick-slip.

correct the stress measurements for the reduction of contact area along the saw-cut as a function of load-point displacement (Fig. S6). We also estimate the uncertainties caused by the evolution of normal stress during velocity steps (Supplementary Text S2 and Fig. S7).

The mechanical data of Pelona, Portal, and Rand Mountain schists under high pressure-high temperature conditions show distinct frictional behavior with significant dependency on ambient temperature and slip rate (Fig. 4). In general, two consecutive sequences of velocity steps display similar frictional properties. The frictional resistance showcases work-hardening over multiple velocity steps due to progressive gouge evolution, a common effect in triaxial deformation experiments, and is corrected for in our analysis (Supplementary Text S1). At temperatures below 300 °C and slip-rates greater than 1 µm/s, all schist samples exhibit a frictional behavior with a slip-rate and state dependence. The direct effect manifests itself gradually due to the sample and machine stiffness and is followed by an evolutionary phase to a new steady-state frictional level. In the frictional regime, the evolutionary phase compensates the direct effect partially.

We analyze the mechanical data using the RSFit3000 methodology (Skarbek and Savage, 2019) based on an empirical friction law (Ruina, 1983; Dieterich, 1979) (Supplementary Text S1). The empirical model explains the mechanical data well using the aging law or slip law (Figs. S8, S9, and S10). Particularly, we focus on the temperature and slip-rate dependence of the direct effect and steady-state parameters

$$a = \frac{\partial \mu}{\partial \ln V}$$
$$a - b = \frac{\partial \mu_{ss}}{\partial \ln V}\,, \tag{1}$$

where μ is the friction coefficient, μ_{ss} is the steady-state friction coefficient, measured when the evolutionary effects have dissipated, and V is the instantaneous slip-rate. Fit with the empirical law also provides the characteristic weakening distance L for the evolutionary effect. The best-fitting parameters a, $a-b$, and L for the PLS2, POS, and RM5 samples are shown in Figs. 5 and 6 for the aging law and in Figs. S11 for the slip law.

The experimental data of Pelona schist sample PLS2, with its 40 wt% chlorite content, displays three distinct mechanical regimes strongly

dependent on temperature and slip-rate. The direct effect parameter increases with slip-rate above 300 °C (Figs. 5d and 6a,c). Pelona schist sample PLS2 displays slip-rate- and state-dependent friction at 100 °C with a velocity-strengthening to velocity-weakening transition around 200 °C followed with increasing temperature by a transition to velocity-strengthening deformation at about 300 °C. At high-temperature, from 400 °C to 500 °C, the mechanical response of Pelona schist features a greater dependence on slip-rate with a direct effect parameter as high as $a = 2.5 \times 10^{-2}$ (Figs. 5d and 6c). The critical slip distance becomes increasingly variable with increasing temperature.

Portal schist sample POS, more quartz-rich and with a contribution of chlorite and biotite, displays a friction coefficient of ~ 0.5 at all temperatures, the lowest among the three samples. We observe a slight dependency of the friction coefficient and direct effect parameter with increasing temperature around 400-500 °C (Figs. 4 and 6e,f,g). POS displays velocity-weakening behavior between 300 °C and 450 °C, but only at low slip-rates. POS features steady-state velocity-strengthening friction at 100-300 °C with a transition to velocity-weakening around 400 °C followed by a second transition to velocity-strengthening deformation at about 500 °C, depending on slip-rate (Fig. 6h). Despite some variability, the characteristic weakening distance does not appear to be a strong function of temperature or slip rate.

The Rand schist sample RM5, consisting mainly of amphibole, chlorite, epidote, and albite, and notably a small amount of quartz, is velocity-strengthening at all conditions considered. RM5 exhibits the highest friction coefficient among 3 samples without discernable temperature dependence (Fig. 6i,j). The mechanical response is systematically velocity-strengthening at steady-state in the experimental conditions considered (Fig. 6l). The characteristic weakening distance exhibits no obvious pattern with temperature or slip-rate.

4. Physical model and constitutive parameters

To better understand the physics underpinning the frictional properties of POR schists, we calibrate a constitutive model of fault friction against the mechanical data in Fig. 6. The constitutive relationship combines frictional sliding and a thermally activated rate-dependent plastic deformation mechanism. The frictional resistance originates from the real area of contact formed by micro-asperities (Bowden and Tabor, 1950; Dieterich and Kilgore, 1994; Baumberger et al., 1999; Barbot, 2024c; Wu and Barbot, 2025). The real area of contact density is controlled by stress and micro-asperity size following the relationship (Barbot, 2019, 2024a)

$$\mathcal{A} = \frac{\sigma}{\chi_n}\left(\frac{d}{d_0}\right)^{\alpha}\left(\frac{\sigma}{\sigma_0}\right)^{-\beta}, \tag{2}$$

where σ and $\sigma_0 = 200$ MPa are the effective normal stress and a reference value, respectively, χ_n is a scaling factor commensurate with the indentation hardness, d and $d_0 = 1$ μm are the size of micro-asperities and a reference value, respectively, and α and β are power-law exponents. The frictional strength is given by $\tau_y = \mathcal{A}\chi$, where χ scales with the plowing hardness. The combined effect of the two deformation mechanisms can be expressed as (Barbot, 2023, 2024b)

$$\frac{V}{V_0} = \left(\frac{\tau}{\tau_y}\right)^{n_1}\exp\left[-\frac{Q_1}{R}\left(\frac{1}{T}-\frac{1}{\bar{T}_1}\right)\right] + \left(\frac{\tau}{\tau_0}\right)^{n_2}\exp\left[-\frac{Q_2}{R}\left(\frac{1}{T}-\frac{1}{\bar{T}_2}\right)\right], \tag{3}$$

where V and $V_0 = 1$ μm/s are the instantaneous and reference sliding velocities, respectively, τ represents the norm of the shear traction, τ_0 is a constant reference value, and the n_k are power-law exponents. While the first power-law term on the right-hand side of Equation (3) with $n_1 \gg 1$ corresponds to slip-rate and state-dependent deformation via the evolving real area of contact, the second power-law term captures strictly slip-rate-dependent, inherently rate-strengthening deformation. The combination of two flow laws captures the brittle-to-flow transition as a function of temperature and slip-rate (Reinen et al., 1992, 1994; Barbot and Zhang, 2023; Barbot, 2024b). The use of power laws retains the physical interpretation of τ_y as a yield strength and regularizes the constitutive behavior at vanishing slip-rates (Barbot, 2019). The thermodynamic parameters Q_k and $\bar{T}_k$ are the activation energy and activation temperature, respectively, with the universal gas constant R. As experiments are conducted at constant effective normal stress, we ignore the pressure dependence of the activation temperature (Barbot et al., 2025). The normalizing parameters d_0, σ_0, and V_0 are introduced to feature power-laws of non-dimensional quantities. Only the product of all reference parameters weighted by their respective power can be constrained by the data. The choice of individual reference parameters does not affect the rheological behavior.

The constitutive framework includes an evolution law for the size of micro-asperities (Barbot, 2022, 2024b)

$$\frac{d}{d_0} = \sum_{k=1}^{N}\frac{f_0}{p_k}\left(\frac{d}{d_0}\right)^{-p_k}\left(\frac{\sigma}{\sigma_0}\right)^{q_k}\exp\left[-\frac{H_k}{R}\left(\frac{1}{T}-\frac{1}{T_k}\right)\right] - \frac{\lambda V}{2h} \tag{4}$$

compatible with the aging law, or another similar expression compatible with the slip-law end-member, where $N = 2$ is the number of competing healing mechanisms characterized with the power-law exponents p_k and q_k, the reference strain rate $f_0 = 1/\text{s}$, and the activation enthalpy and activation temperature H_k and T_k, respectively. The shear zone thickness $h = 1$ mm corresponds to the gouge thickness in the vessel, and $1/\lambda$ is a characteristic strain for weakening. The model employs a single state variable, the size of micro-asperities, which is sufficient to capture the steady-state velocity-strengthening and velocity-weakening regimes at different temperatures and slip-rates (e.g., Nie and Barbot, 2024).

To explain the mechanical data in Fig. 4, we simulate velocity steps numerically using a spring-slider assembly with infinite stiffness, where the slider obeys the constitutive laws of Equations (3) and (4). For each velocity step, we assume that the mechanical system is at steady-state at velocity V_1, followed by a sudden change of loading rate to a velocity V_2, taking the values of 1.22, 0.244, and 0.0488 μm/s, as the slip-rate at the interface is 22% higher than the axial loading due to the saw-cut geometry at 35°.

The constitutive equations do not afford closed-form solutions for the steady state, so we resort to numerical solutions. We calculate the evolution of the frictional strength using a fifth-order accurate Runge-Kutta method (Press et al., 1992). We evaluate the effective frictional parameters using Equation (1) with the synthetic data. We use a pair-wise grid search to determine the best-fitting constitutive parameters (Fig. S12). The prediction of the constitutive model is shown as background color in Fig. 6, showing an overall good agreement with the empirical parameters.

The experimental data for PLS2 is captured by the constitutive framework using the parameters in Table S1. Specifically, the transition from steady-state velocity-strengthening at 100 °C to velocity-weakening at 180 °C can be explained by the competition between two healing mechanisms with activation energies $H_1 = 40$ kJ/mol and $H_2 = 80$ kJ/mol and activation temperatures $T_1 = 0$ °C and $T_2 = 180$ °C, with power-law exponents $p_1 = 9.0$ and $p_2 = 3.3$. The semi-brittle regime that activates at 300 °C is characterized by a thermally activated power-law relationship with the stress power exponent $n_2 = 70$, the activation energy $Q_2 = 150$ kJ/mol, and an activation temperature $\hat{T}_2 = 650$ °C.

For POS, the transition from steady-state velocity-strengthening at 300 °C to velocity-weakening at 400 °C is captured by the switch of dominant healing mechanism, characterized by the activation energies $H_1 = 25$ kJ/mol and $H_2 = 60$ kJ/mol, and the power exponents $p_1 = 5.0$ and $p_2 = 1.8$. The transition to a semi-brittle, velocity-strengthening regime around ~ 400 °C and ~ 500 °C depending on slip-rate can be explained with the activation of the second deformation mechanism with stress exponent $n_2 = 32$, activation energy $Q_2 = 90$ kJ/mol and activation temperature $\bar{T}_2 = 900$ °C.

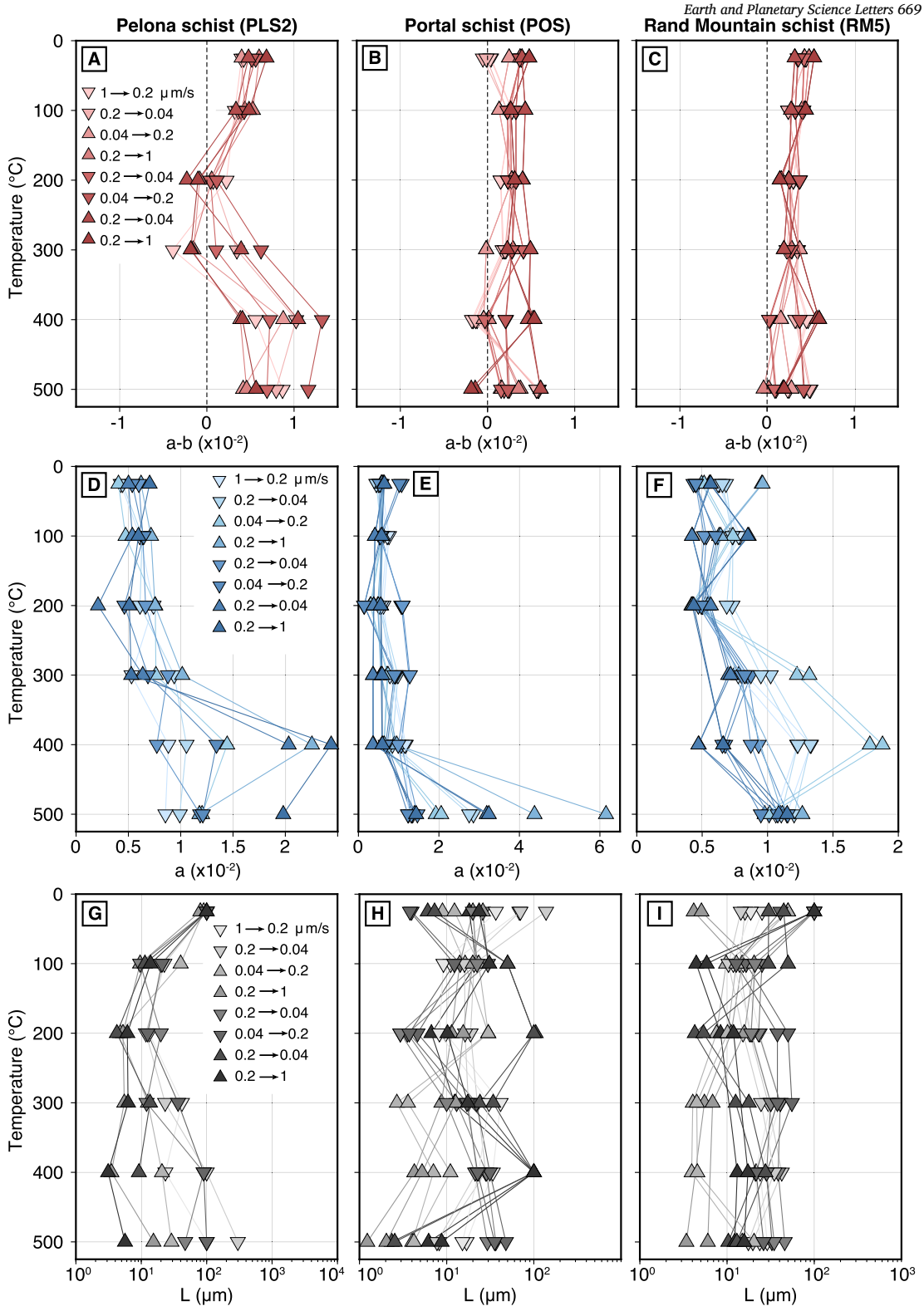

Fig. 5. Evolution of effective frictional properties with temperature and slip-rate using aging law. a, b, c) Velocity-dependence of the steady-state coefficient of friction for PLS2, POS, and RM5, respectively. d, e, f) Direct velocity-dependence of the coefficient of friction for PLS2, POS, and RM5 as a function of temperature and slip-rate. g, h, i) Characteristic weakening distance for PLS2, POS, and RM5 as a function of temperature and slip-rate.

For RM5, the frictional behavior is modeled with $\mu_0 = 0.65$, the activation energies for healing of $H_1 = 25\,\text{kJ/mol}$ and $H_2 = 70\,\text{kJ/mol}$, with exponents $p_1 = 7.6$ and $p_2 = 3.6$. The Rand Mountain schist, consisting mainly of amphibole, chlorite, epidote, and albite, is velocity-strengthening in all considered conditions (Fig. 6g). All the constitutive parameters are shown in Table S1. In all cases above, we assume a reference velocity $V_0 = 1\,\mu\text{m/s}$, a reference micro-asperity size $d_0 = 1\,\mu\text{m}$, and a reference normal stress $\sigma_0 = 200\,\text{MPa}$. The physical model does not underpredict the strength at high temperature for any of the samples.

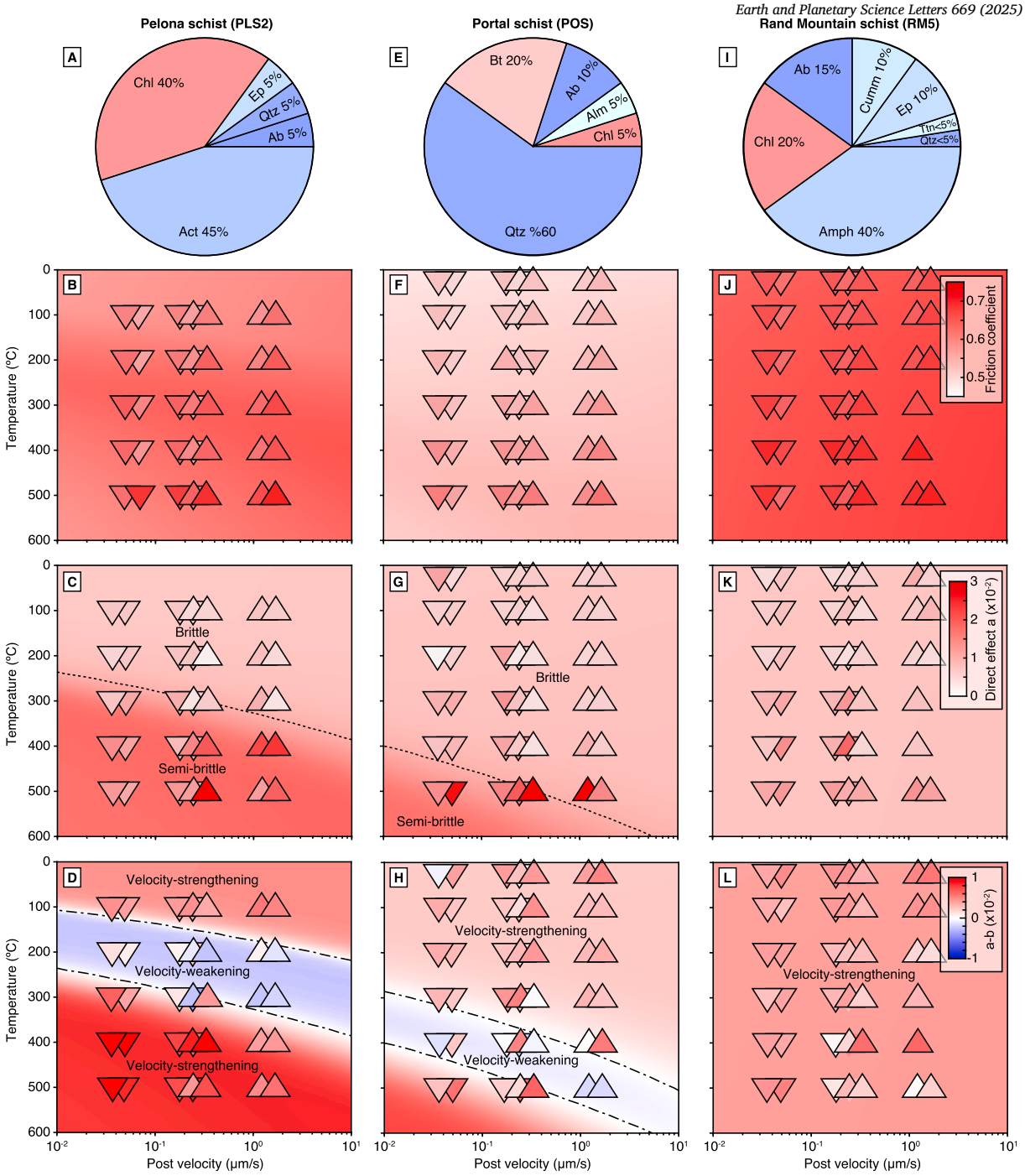

Fig. 6. Mineral composition of selected samples and corresponding frictional properties as a function of temperature and slip-rate. a, e, i) Relative abundance of minerals (Table 1) in PLS2, POS and RM5, respectively. The phyllosilicate minerals chlorite (Chl) and biotite (Bt) are colored in shades of red. Other minerals displayed in shades of blue by abundance. The upward and downward triangles indicate measurements from up and down steps, respectively. The data for the second velocity-step sequence is offset for convenience. b, c, d) Frictional properties of PLS2. f, g, h) Frictional properties of POS. j, k,l) Frictional properties of RM5. The top panels b,f,j) indicate the evolution of the friction coefficient at the onset of velocity steps. Increasing values at the same temperature and slip-rate represent work hardening. The middle panels c,g,k) show the distribution of the direct effect parameter a. The bottom panels d,h,l) show the steady-state velocity dependence parameter $a - b$. The background indicates the prediction of the constitutive model presented in Section 4.

The laboratory data and associated physical model provide a robust explanation for the stability of POR schists above 300-500 °C (Fig. 7). We model the evolution of the frictional resistance upon velocity steps using a spring-slider system with a stiffness of 0.2 MPa/μm, where the slider obeys the constitutive framework described above. For the actinolite- and chlorite-rich PLS2, the frictional response to velocity steps includes a direct effect and an evolutionary phase converging to a new steady-state strength after a slip of 200 μm. This mechanical response is characteristic of slip-rate- and state-dependent friction. Although the steady-state strength depends on temperature, the direct effect remains relatively constant. This behavior implies constancy of the deformation mechanism, characterized by a single stress power-law exponent. While a single shear deformation mechanism dominates, a switch of dominant healing mechanism leads to a transition from stable steady-state friction at 25 °C to unstable friction at 300 °C. The thermal activation of healing mechanisms in the constitutive model captures

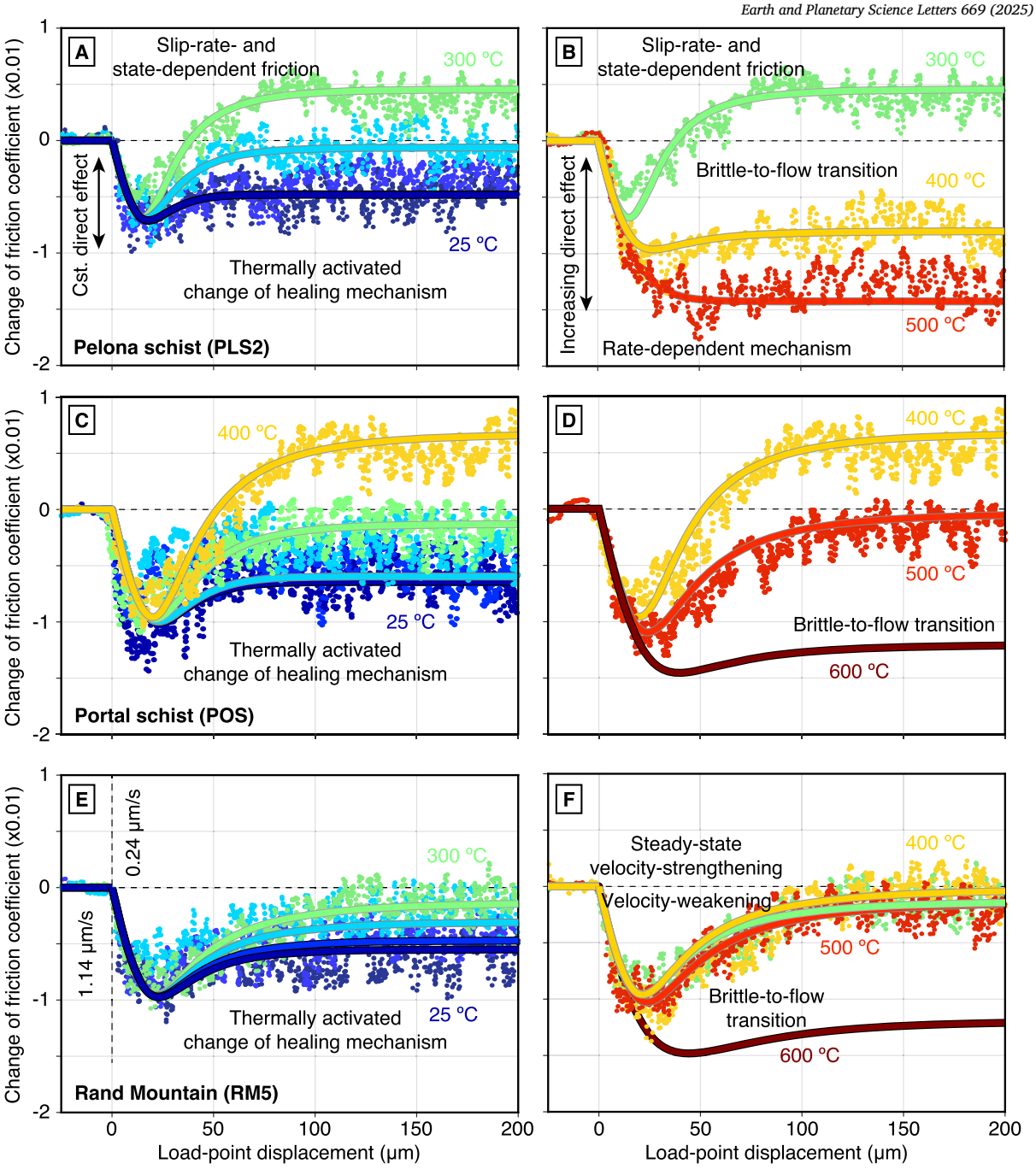

Fig. 7. Regimes of frictional stability of POR schists during velocity down-steps from 1.14 µm/s to 0.24 µm/s. a) Thermally activated transition between steady-state velocity-strengthening friction at 25-100°C to velocity-weakening at 300°C occurring under relatively constant direct effect for Pelona schist sample PLS2. b) Thermally activated brittle-to-flow transition characterized by a steady-state velocity-weakening slip-rate- and state-dependent frictional response at 300°C evolving to an inherently stable rate-dependent response at 500°C for PLS2. The solid line represents the prediction of the physical model described in Section 4. c) Thermally activated stable to unstable transition in the brittle regime for Portal schist sample POS. d) Brittle-to-flow transition from 400°C to 500°C for sample POS. The model prediction for 550°C indicates a more complete transition to rate-dependent creep at high temperatures. e) Thermally activated variations of steady-state frictional resistance of Rand Mountain schist (RM5), approaching velocity-neutral at 300°C. f) Increased stability sample RM5 at high temperatures. The model prediction at 600°C indicates the brittle-to-flow transition.

the laboratory observations well. From 300 °C to 500 °C, the mechanical response to velocity steps features an increased direct effect and a transition to velocity-strengthening, compatible with a transition from slip-rate- and state-dependent friction to rate-dependent deformation with limited evolutionary effects. The gradual change of strength for the velocity step at 500 °C (Fig. 7b) is caused by the stiffness of the machine-sample assembly, not by an evolutionary effect. A similar transition occurs in synthetic actinolite-chlorite gouge between 100 °C and 200 °C in rotary shear experiments conducted at 50, 100, and 200 MPa effective normal stress (Okamoto et al., 2020), and the phenomenon can be observed for a wide range of rocks (Barbot, 2024b).

The constitutive model captures this transition by the thermal activation of the second deformation mechanism characterized by a different stress power-law exponent. Similar phenomena may occur for all POR samples. For POS, the transition from slip-rate- and state-dependent friction to rate-dependent creep initiates at 400 °C. The constitutive model

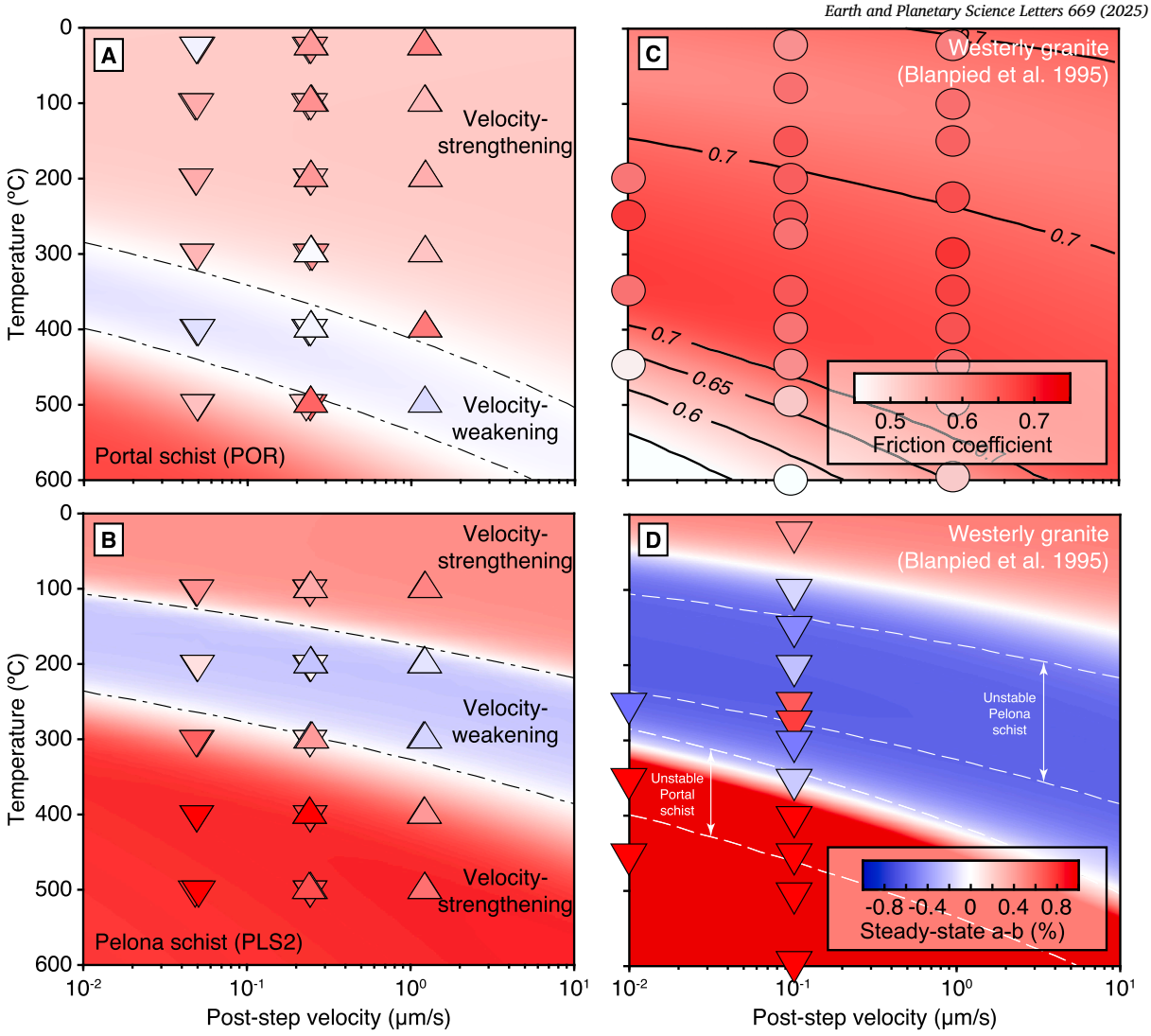

Fig. 8. Comparison of the frictional stability regimes of POS, PLS2, and Westerly granite in hydrothermal conditions. a) Steady-state velocity dependence of POR friction as a function of temperature and slip-rate. b) Velocity dependence of PLS2 friction as a function of temperature and slip-rate. The background color corresponds to the constitutive law presented in Section 4 with the parameters in Table S1. c) Friction coefficient of Westerly granite (Blanpied et al., 1995). d) Steady-state velocity dependence of Westerly granite friction (Blanpied et al., 1995). The background corresponds to the constitutive model with the best-fitting parameters for Westerly granite (Barbot, 2023). The downward and upward triangles indicate laboratory measurements during down-steps and up-steps during the second sequence, respectively.

predicts a complete transition to rate-dependent creep at 550 °C, outside the experimental range. For RM5, the transition from slip-rate- and state-dependent friction to rate-dependent creep initiates at 300 °C and would complete at temperatures above 600 °C, as shown by the constitutive model. Hence, despite apparent differences in slip-rate and temperature ranges of stability, the samples experience similar underlying phenomena, albeit with different constitutive parameters. The stability of POR schists above 500 °C originates from a thermally activated transition to rate-dependent creep.

5. Discussion

The mechanical response to velocity steps of POR schists under identical laboratory conditions varies due to differences in mineralogy. Although XRD analysis classifies RM5 and PLS2 as chlorite-amphibole schists, some compositional differences persist. PLS2 contains substantially more chlorite and forms a phyllosilicate-rich matrix. RM5, in contrast, is dominated by amphibole and albite, with significantly less quartz and chlorite. The consistent velocity-strengthening behavior of RM5 may be associated with its lower quartz content, distinguishing it from the POS and PLS2 samples. PLS2 displays more complex mechanical behavior, with a steady-state velocity-weakening regime between 150 °C and 350 °C depending on slip-rate, presumably reflecting the properties of chlorite and actinolite. Synthetic chlorite-actinolite mixtures feature steady-state velocity-weakening friction between 200 °C and 300 °C at low pore-fluid and confining pressure and high slip-rate conditions (Okamoto et al., 2020), showing similarities with chlorite- and actinolite-rich PLS2 at various effective normal stress conditions (Barbot et al., 2025). Further experimental work is required to better constrain the individual frictional properties of the constituent minerals of POR schist, particularly chlorites, amphiboles, and feldspars. The distinct mineral assemblages of POS, RM5, and PLS2 revealed by XRD and thin section analyses highlight the heterogeneity of POR schists, even within similar metamorphic range. Variations in phyllosilicate, quartz, feldspar, and amphibole content due to different protoliths and metamorphic grades leads to distinct frictional properties, with substantial implications for fault stability in the middle and lower crust.

To better understand how these lithological variations impact fault mechanics, we compare PLS2 and POS schist samples to Westerly granite (Blanpied et al., 1995), a monzogranite typically composed of 27-

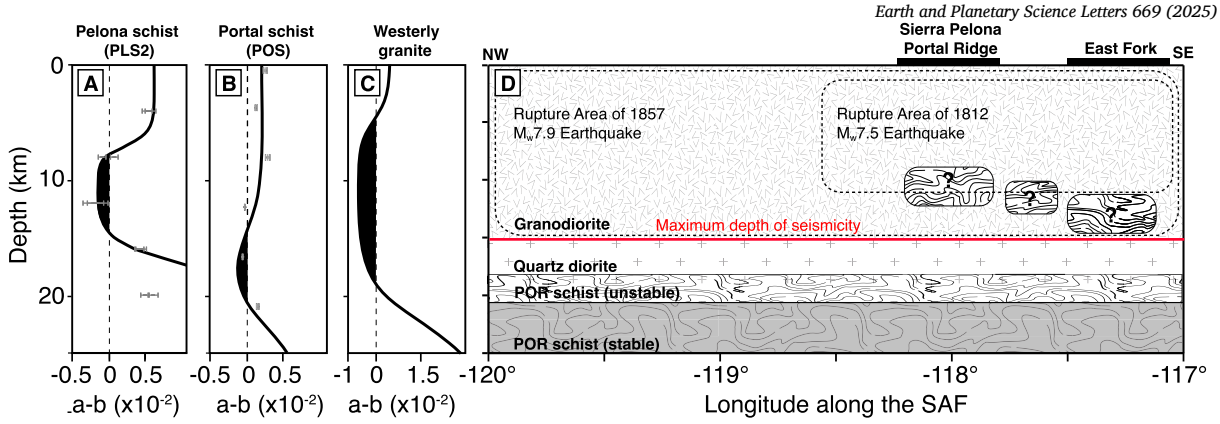

Fig. 9. Depth distribution of the slip-rate- and state-dependent friction parameters and lithology. a, b, c) The depth distribution of the slip-rate- and state-dependent friction parameters $(a - b)$ for PLS2, POS, and Westerly granite. d) Vertical along-strike cross section showing hypothetical rupture areas of 1857 Mw 7.9 and 1812 Mw 7.5 earthquakes (Lozos, 2016; Hauksson et al., 2024). Maximum depth of seismicity (red solid line) and a conceptual cross-section derived from the Community Rheology Model (Hearn et al., 2020). Black dashed boxes mark rupture areas of the 1857 Mw 7.5 San Juan Capistrano and 1812 Mw 7.9 Fort Tejon earthquakes. Gray shaded area indicates the depth range where POR schist is frictionally stable. The locations of the Sierra Pelona and East Fork outcrops are marked by red boxes at the surface.

30 wt% quartz, 35-40 wt% microcline, 29-33 wt% plagioclase, 1-2 wt% muscovite, and 2-3 wt% biotite that serves as a well-characterized representative of strong, felsic upper crustal lithologies (Fig. 8). Because granite is a common and volumetrically significant component of the continental upper crust, Westerly granite serves as a useful experimental benchmark for comparing the frictional behavior of fault rocks like the POR schists to that of a typical, strong crustal endmember. The constitutive model explaining the mechanical behavior of Westerly granite (Blanpied et al., 1995) under an effective normal stress of 400 MPa, including a 100 MPa pore-fluid pressure, can be found in Barbot (2023). Pelona schist, Portal schist, and Westerly granite exhibit three frictional stability regimes with an unstable regime occurring at different ranges of temperature and slip-rate. Westerly granite and Pelona schist exhibit velocity-weakening behavior between 50–450 °C and 100–350 °C, respectively, depending on slip-rate (Fig. 8). This critical transition from velocity-strengthening to velocity-weakening over similar temperature ranges suggests that both lithologies may contribute to upper-crustal seismicity. In contrast, Portal schist shows velocity-weakening behavior at higher temperatures, from 300 °C to 400 °C, potentially enabling seismicity at deeper crustal levels.

The frictionally unstable ranges of granite and some POR schists overlap, complicating direct associations between seismicity and specific lithologies in the brittle crust. POR schists may influence rupture behavior along the Mojave section of the San Andreas Fault, where they crop out at Sierra Pelona, Portal Ridge, and East Fork. The 1812 Mw 7.5 and the 1857 Mw 7.9 earthquakes ruptured through potentially frictionally unstable POR schist at middle-crustal depths (Fig. 9) (Lozos, 2016; Hauksson et al., 2024). The CRM lithology model indicates a prevalent schist basement at 18 km depth. The frictionally stable regime of all POR schists at and above 500 °C indicates a maximum depth of seismicity of 20 km, compatible with seismological observations in the region (Hauksson et al., 2012).

6. Conclusion

The frictional properties of Pelona, Portal, and Rand schists provide new insights into their potential effects on seismicity. In general, the lower limit of seismicity is not a robust marker for the upper boundary of POR schists, as their frictional properties vary with composition. Pelona schist, with its velocity-weakening behavior at low temperatures between 100 °C and 200 °C at low slip-rates, may contribute to seismic events at shallow depths along the Mojave section of the San Andreas Fault. Portal schist enables frictional instabilities in deeper fault segments with a velocity-weakening regime at higher temperatures between 300 °C and 400 °C. All POR schists, however, are frictionally stable at and above 500 °C. The high-temperature stability regime of POR schists is caused by a mechanical transition between slip-rate- and state-dependent friction at low temperature to rate-dependent plasticity at high temperature. In the rate-dependent plasticity regime, state evolution is negligible, resulting in inherently stable slip.

The similarities in velocity-weakening behavior between Westerly granite and some POR schists indicate that both rock types may contribute to seismicity at shallow depths. In contrast, Rand schist, with its velocity-strengthening behavior at all tested temperatures, contributes to aseismic deformation and mechanical stability at shallow and intermediate depths, reducing the likelihood of earthquake initiation where this lithology dominates.

The exploration of POR schist frictional properties underscores the critical importance of considering lithological variations when assessing seismic hazards, as the lithological variability of the continental crust in Southern California influences the extent and depth of the seismogenic zone.

Open research

Data archiving at zenodo.org is underway. A copy of the data is available as Supporting Information.

CRediT authorship contribution statement

S.E. Guvercin: Writing – original draft, Investigation, Data curation, Conceptualization. **S. Barbot:** Writing – original draft, Visualization, Supervision, Methodology, Investigation, Data curation, Conceptualization. **L. Zhang:** Data curation. **Z. Yang:** Data curation. **J. Platt:** Writing – review & editing, Supervision, Investigation. **C. Seyler:** Investigation. **N. Phillips:** Investigation.

Declaration of competing interest

The authors declare that they have no known competing financial interests or personal relationships that could have appeared to influence the work reported in this paper.

Acknowledgements

We are grateful for the technical support of Prof. Changrong He at the Institute of Geology, China Earthquake Administration. The study is funded by the National Science Foundation under award EAR-1848192

and by the National Natural Science Foundation of China under grant 42274234.

Appendix A. Supplementary material

Supplementary material related to this article can be found online at https://doi.org/10.1016/j.epsl.2025.119573.

Data availability

Data will be made available on request.

References

Barbot, S., 2019. Modulation of fault strength during the seismic cycle by grain-size evolution around contact junctions. Tectonophysics 765, 129–145. https://doi.org/10.1016/j.tecto.2019.05.004.

Barbot, S., 2020. Frictional and structural controls of seismic super-cycles at the Japan trench. Earth Planets Space 72 (63). https://doi.org/10.1186/s40623-020-01185-3.

Barbot, S., 2022. A rate-, state-, and temperature-dependent friction law with competing healing mechanisms. J. Geophys. Res. B025, 106. https://doi.org/10.1029/2022JB025106.

Barbot, S., 2023. Constitutive behavior of rocks during the seismic cycle. AGU Adv. 4 (5). https://doi.org/10.1029/2023AV000972.

Barbot, S., 2024a. Transient and steady-state friction in non-isobaric conditions. Geochem. Geophys. Geosyst. 25 (2), e2023GC011. https://doi.org/10.1029/2023GC011279.

Barbot, S., 2024b. Does the direct effect of friction increase continuously with absolute temperature? Proc. Natl. Acad. Sci. USA 121 (42), e2405111. https://doi.org/10.1073/pnas.2405111121.

Barbot, S., 2024c. The slip-rate, state-, temperature-, and normal-stress-dependence f fault friction. Earthq. Sci. 32, 1–35. https://doi.org/10.1016/j.eqs.2025.03.005.

Barbot, S., Zhang, L., 2023. Constitutive behavior of olivine gouge across the brittle-ductile transition. Geophys. Res. Lett. 50 (24). https://doi.org/10.1029/2023GL105916.

Barbot, S., Lapusta, N., Avouac, J.P., 2012. Under the hood of the earthquake machine: towards predictive modeling of the seismic cycle. Science 336 (6082), 707–710. https://doi.org/10.1126/science.1218796.

Barbot, S., Guvercin, S., Zhang, L., Zhang, H., Yang, Z., 2025. Thermobaric activation of fault friction. Geophys. Res. Lett. 52 (6). https://doi.org/10.1029/2024GL112959.

Baumberger, T., Berthoud, P., Caroli, C., 1999. Physical analysis of the state- and rate-dependent friction law. II. Dynamic friction. Phys. Rev. B 60 (6), 3928–3939.

Blanpied, M., Marone, C., Lockner, D., Byerlee, J., King, D., 1998. Quantitative measure of the variation in fault rheology due to fluid-rock interactions. J. Geophys. Res. 103 (B5), 9691–9712. https://doi.org/10.1029/98JB00162.

Blanpied, M.L., Lockner, D.A., Byerlee, J.D., 1995. Frictional slip of granite at hydrothermal conditions. J. Geophys. Res. 100 (B7), 13,045–13,064. https://doi.org/10.1029/95JB00862.

Bowden, F.P., Tabor, D., 1950. The Friction and Lubrication of Solids, Part I. Clarendon Press, Oxford.

Carpenter, B., Marone, C., Saffer, D., 2009. Frictional behavior of materials in the 3d safod volume. Geophys. Res. Lett. 36 (5). https://doi.org/10.1029/2008GL036660.

Carpenter, B., Saffer, D., Marone, C., 2012. Frictional properties and sliding stability of the San Andreas fault from deep drill core. Geology 40 (8), 759–762.

Carpenter, B., Saffer, D., Marone, C., 2015. Frictional properties of the active San Andreas fault at SAFOD: implications for fault strength and slip behavior. J. Geophys. Res. 120 (7), 5273–5289. https://doi.org/10.1002/2015JB011963.

Carpenter, M., Williams, J.N., Fagereng, Å., Wedmore, L.N., Biggs, J., Mphepo, F., Mdala, H., Dulanya, Z., Manda, B., 2022. Comparing intrarift and border fault structure in the Malawi rift: implications for normal fault growth. J. Struct. Geol. 165, 104761. https://doi.org/10.1016/j.jsg.2022.104761.

Chapman, A.D., 2016. The pelona–orocopia–rand and related schists of Southern California: a review of the best-known archive of shallow subduction on the planet. Int. Geol. Rev. 59 (5–6), 664–701. https://doi.org/10.1080/00206814.2016.1230836.

Chapman, A.D., Kidder, S., Saleeby, J.B., Ducea, M.N., 2010. Role of extrusion of the rand and Sierra de Salinas schists in late Cretaceous extension and rotation of the Southern Sierra Nevada and vicinity. Tectonics 29 (5). https://doi.org/10.1029/2009TC002597.

Christensen, N., Mooney, W., 1995. Seismic velocity structure and composition of the continental crust: a global view. J. Geophys. Res., Solid Earth 100 (B7), 9761–9788. https://doi.org/10.1029/95JB00259.

den Hartog, S., Niemeijer, A., Spiers, C.J., 2012. New constraints on megathrust slip stability under subduction zone P–T conditions. Earth Planet. Sci. Lett. 353, 240–252.

Dieterich, J.H., 1979. Modeling of rock friction 1. Experimental results and constitutive equations. J. Geophys. Res. 84 (B5), 2161–2168. https://doi.org/10.1029/JB084iB05p02161.

Dieterich, J.H., Kilgore, B.D., 1994. Direct observation of frictional contacts: new insights for sliding memory effects. Pure Appl. Geophys. 143, 283–302. https://doi.org/10.1007/BF00874332.

Eymold, W.K., Jordan, T.H., 2019. Tectonic regionalization of the Southern California crust from tomographic cluster analysis. J. Geophys. Res., Solid Earth 124 (11), 11,840–11,865. https://doi.org/10.1029/2019JB018423.

Field, E.H., Milner, K.R., Hardebeck, J.L., Page, M.T., van der Elst, N., Jordan, T.H., Michael, A.J., Shaw, B.E., Werner, M.J., 2017. A spatiotemporal clustering model for the third uniform California earthquake rupture forecast (UCERF3-ETAS): toward an operational earthquake forecast. Bull. Seismol. Soc. Am. 107 (3), 1049–1081. https://doi.org/10.1785/0120160173.

Fuis, G.S., Murphy, J.M., Baher, S., Ryberg, T., Kohler, M.D., Okaya, D.A., 2005. Lithospheric refraction/reflection/teleseismic model of larse line 2: thrusting of the Santa monica mountains-san Fernando valley block beneath the central transverse ranges, Southern California. Eos Trans. AGU 86 (52). Fall Meet. Suppl., Abstract S41A–0971.

Grove, M., Bebout, G.E., 1995. Cretaceous tectonic evolution of coastal Southern California: insights from the Catalina schist. Tectonics 14 (6), 1290–1308. https://doi.org/10.1029/95TC01931.

Grove, M., Jacobson, C.E., Barth, A.P., Vucic, A., 2003. Temporal and spatial trends of late Cretaceous-early tertiary underplating pelona and related schist beneath Southern California and southwestern Arizona. In: Tectonic Evolution of Northwestern Mexico and the Southwestern USA. Geological Society of America.

Hauksson, E., Yang, W., Shearer, P.M., 2012. Waveform relocated earthquake catalog for Southern California (1981 to June 2011). Bull. Seismol. Soc. Am. 102 (5), 2239–2244. https://doi.org/10.1785/0120120010.

Hauksson, E., Jones, L.M., Stock, J.M., Husker, A.L., 2024. Synthesis of current seismicity and tectonics along the 1857 mw7. 9 fort tejon earthquake rupture and the southernmost San Andreas fault, California, USA. J. Geophys. Res., Solid Earth 129 (6), e2024JB028893.

Hawkesworth, C., Kemp, A., 2006. Evolution of the continental crust. Nature 443, 811–817. https://doi.org/10.1038/nature05191.

He, C., Yao, W., Wang, Z., Zhou, Y., 2006. Strength and stability of frictional sliding of gabbro gouge at elevated temperatures. Tectonophysics 427 (1–4), 217–229. https://doi.org/10.1016/j.tecto.2006.05.023.

Hearn, E., Montesi, L., Oskin, M., Hirth, G., Thatcher, W., Behr, W., 2020. SCEC Community Rheology Model (CRM) (20.9).

Hirauchi, K.-i., Yamamoto, Y., den Hartog, S.A., Niemeijer, A.R., 2020. The role of metasomatic alteration on frictional properties of subduction thrusts: an example from a serpentinite body in the franciscan complex, California. Earth Planet. Sci. Lett. 531, 115,967. https://doi.org/10.1016/j.epsl.2019.115967.

Ikari, M.J., Saffer, D.M., Marone, C., 2009. Frictional and hydrologic properties of clay-rich fault gouge. J. Geophys. Res. 114 (B5).

Jacobson, C.E., 1990. The 40ar/39ar geochronology of the pelona schist and related rocks, Southern California. J. Geophys. Res., Solid Earth 95 (B1), 509–528.

Jacobson, C.E., Grove, M., Vucic, A., Pedrick, J.N., Ebert, K.A., 2007. Exhumation of the orocopia schist and associated rocks of southeastern California: relative roles of erosion, synsubduction tectonic denudation, and middle Cenozoic extension. https://doi.org/10.1130/2007.2419(01).

Jenkins, O.P., 1977. Geologic Map of California.

Julve, J., Barbot, S., Moreno, M., Tassara, A., Araya, R., Catalán, N., Crempien, J.G., Becerra-Carreño, V., 2023. Recurrence time and size of Chilean earthquakes influenced by geological structure. Nat. Geosci., 1–9. https://doi.org/10.1038/s41561-023-01327-8.

Julve, J., Moreno, M., Barbot, S., Tassara, A., 2025. Impact of upper-plate faulting on megathrust foreshocks: insights from the 2014 Iquique earthquake. Geophys. Res. Lett. 52 (3), e2024GL111064. https://doi.org/10.1029/2024GL111064.

Lee, E.-J., Chen, P., Jordan, T.H., Maechling, P.B., Denolle, M.A., Beroza, G.C., 2014. Full-3-d tomography for crustal structure in Southern California based on the scattering-integral and the adjoint-wavefield methods. J. Geophys. Res., Solid Earth 119 (8), 6421–6451. https://doi.org/10.1002/2014JB011346.

Lei, H., Niemeijer, A.R., Zhou, Y., Spiers, C.J., 2024. Frictional properties of natural granite fault gouge under hydrothermal conditions: a case study of strike-slip fault from anninghe fault zone, southeastern Tibetan Plateau. J. Geophys. Res. 129 (8), e2024JB028760. https://doi.org/10.1029/2024JB028760.

Lozos, J., 2016. A case for historic joint rupture of the San Andreas and san jacinto faults. Science. https://doi.org/10.1126/sciadv.1500621.

Magistrale, H., Zhou, H.-w., 1996. Lithologic control of the depth of earthquakes in Southern California. Science 273 (5275), 639–642. https://doi.org/10.1126/science.273.5275.639.

Moore, D.E., Lockner, D.A., 2011. Frictional strengths of talc-serpentine and talc-quartz mixtures. J. Geophys. Res. 116 (B1). https://doi.org/10.1029/2010JB007881.

Moore, D.E., Lockner, D.A., Hickman, S., 2016. Hydrothermal frictional strengths of rock and mineral samples relevant to the creeping section of the San Andreas fault. J. Struct. Geol. 89, 153–167. https://doi.org/10.1016/j.jsg.2016.06.005.

Nazareth, J.J., Hauksson, E., 2004. The seismogenic thickness of the Southern California crust. Bull. Seismol. Soc. Am. 94 (3), 940–960. https://doi.org/10.1785/0120020129.

Nie, S., Barbot, S., 2024. Velocity and temperature dependence of steady-state friction of natural gouge controlled by competing healing mechanisms. Geophys. Res. Lett. https://doi.org/10.1029/2024GL123456.

Niemeijer, A., Boulton, C., Toy, V., Townend, J., Sutherland, R., 2016. Large-displacement, hydrothermal frictional properties of DFDP-1 fault rocks, Alpine fault, New Zealand: implications for deep rupture propagation. J. Geophys. Res. 121 (2), 624–647. https://doi.org/10.1002/2015JB012593.

Okamoto, A.S., Niemeijer, A.R., Takeshita, T., Verberne, B.A., Spiers, C.J., 2020. Frictional properties of actinolite-chlorite gouge at hydrothermal conditions. Tectonophysics 779, 228,377. https://doi.org/10.1016/j.tecto.2020.228377.

Okuda, H., Katayama, I., Sakuma, H., Kawai, K., 2021. Effect of normal stress on the frictional behavior of brucite: application to slow earthquakes at the subduction plate interface in the mantle wedge. Solid Earth 12 (1), 171–186. https://doi.org/10.5194/se-12-171-2021.

Okuda, H., Niemeijer, A.R., Takahashi, M., Yamaguchi, A., Spiers, C.J., 2023. Hydrothermal friction experiments on simulated basaltic fault gouge and implications for megathrust earthquakes. J. Geophys. Res. 128 (1), e2022JB025,072. https://doi.org/10.1029/2022JB025072.

Porter, R., Zandt, G., McQuarrie, N., 2011. Pervasive lower-crustal seismic anisotropy in Southern California: evidence for underplated schists and active tectonics. Lithosphere 3 (3), 201–220. https://doi.org/10.1130/L126.1.

Press, W.H., Teukolsky, S.A., Vetterling, W.T., Flannery, B.P., 1992. Numerical Recipes in C: The Art of Scientific Computing, 2nd ed. Cambridge Univ. Press, New York. 994 pp.

Reinen, L.A., Tullis, T.E., Weeks, J.D., 1992. Two-mechanism model for frictional sliding of serpentinite. Geophys. Res. Lett. 19 (15), 1535–1538. https://doi.org/10.1029/92GL01388.

Reinen, L.A., Weeks, J.D., Tullis, T.E., 1994. The frictional behavior of lizardite and antigorite serpentinites: experiments, constitutive models, and implications for natural faults. Pure Appl. Geophys. 143, 317–358. https://doi.org/10.1007/BF00874334.

Romanyuk, T., Mooney, W.D., Detweiler, S., 2007. Two lithospheric profiles across Southern California derived from gravity and seismic data. J. Geodyn. 43 (2), 274–307. https://doi.org/10.1016/j.jog.2006.09.011.

Rudnick, R., Gao, S., 2014. Composition of the Continental Crust, vol. 4, 2nd ed. Elsevier. 1-51 pp.

Ruina, A., 1983. Slip instability and state variable friction laws. J. Geophys. Res. 88, 10,359–10,370. https://doi.org/10.1029/JB088iB12p10359.

Saleeby, J., 2003. Segmentation of the laramide slab—evidence from the Southern Sierra Nevada region. Geol. Soc. Am. Bull. 115 (6), 655–668. https://doi.org/10.1130/0016-7606(2003)115<0655:SOTLSF>2.0.CO;2.

Sawai, M., Niemeijer, A.R., Plümper, O., Hirose, T., Spiers, C.J., 2016. Nucleation of frictional instability caused by fluid pressurization in subducted blueschist. Geophys. Res. Lett. 43 (6), 2543–2551. https://doi.org/10.1002/2015GL0675.

Skarbek, R.M., Savage, H.M., 2019. RSFit3000: a MATLAB GUI-based program for determining rate and state frictional parameters from experimental data. Geosphere 15 (5), 1665–1676. https://doi.org/10.1130/GES02122.1.

Tulley, C., Fagereng, Å., Ujiie, K., Diener, J., Harris, C., 2022. Embrittlement within viscous shear zones across the base of the subduction thrust seismogenic zone. Geochem. Geophys. Geosyst. 23 (9), e2021GC010,208. https://doi.org/10.1029/2021GC010208.

Ujiie, K., Noro, K., Shigematsu, N., Fagereng, Å., Nishiyama, N., Tulley, C.J., Masuyama, H., Mori, Y., Kagi, H., 2022. Megathrust shear modulated by albite metasomatism in subduction mélanges. Geochem. Geophys. Geosyst. 23 (8), e2022GC010569. https://doi.org/10.1029/2022GC010569.

Wang, B., Barbot, S., 2024. Rupture segmentation on the East Anatolian fault (Turkey) controlled by along-strike variations in long-term slip rates in a structurally complex fault system. Geology. https://doi.org/10.1130/G52403.1.

Wang, K., Jiang, C., Yang, Y., Schulte-Pelkum, V., Liu, Q., 2020. Crustal deformation in Southern California constrained by radial anisotropy from ambient noise adjoint tomography. Geophys. Res. Lett. 47 (12), e2020GL088580. https://doi.org/10.1029/2020GL088580.

White, M.C.A., Fang, H., Catchings, R.D., Goldman, M.R., Steidl, J.H., Ben-Zion, Y., 2021. Detailed traveltime tomography and seismic catalogue around the 2019 Mw7.1 Ridgecrest, California, earthquake using dense rapid-response seismic data. Geophys. J. Int. 227, 204–227. https://doi.org/10.1093/gji/ggab224.

Wu, B., Barbot, S., 2025. Evolution of the real area of contact during laboratory earthquakes. Proc. Natl. Acad. Sci. https://doi.org/10.1073/pnas.2410496122.

Xia, H., Platt, J.P., 2017. Structural and rheological evolution of the laramide subduction channel in Southern California. Solid Earth 8 (2), 379–403. https://doi.org/10.5194/se-8-379-2017.

Zhang, F., An, M., Zhang, L., Fang, Y., Elsworth, D., 2019. The role of mineral composition on the frictional and stability properties of powdered reservoir rocks. J. Geophys. Res. 124 (2), 1480–1497. https://doi.org/10.1029/2018JB016174.

Zhang, L., He, C., 2013. Frictional properties of natural gouges from Longmenshan fault zone ruptured during the Wenchuan Mw7. 9 earthquake. Tectonophysics 594, 149–164. https://doi.org/10.1016/j.tecto.2013.03.030.